JGR Oceans

RESEARCH ARTICLE

10.1029/2026JC024033

Key Points:

- Oceanic and atmospheric simulations with 100 m horizontal grid spacing showed how local winds affected coastal circulation in a small bay
- Simulated short-timescale local wind variability enhanced bay interior upwelling that improved the simulated SSS distribution
- Upwelling in a small bay can occur not only as coastal or curl-driven upwelling, but also as divergence-driven bay interior upwelling

Supporting Information:

Supporting Information may be found in the online version of this article.

Correspondence to:

Y.-J. Kim,
yoojunkim@aori.u-tokyo.ac.jp

Citation:

Kim, Y.-J., Tanaka, K., Seo, H., Komatsu, K., Matsumura, Y., Sauvage, C., & Renkl, C. (2026). The role of time- and spatially varying wind in coastal circulation based on high-resolution oceanic and atmospheric simulations. *Journal of Geophysical Research: Oceans*, *131*, e2026JC024033. https://doi.org/10.1029/2026JC024033

Received 14 JAN 2026
Accepted 5 AUG 2026

Author Contributions:

Conceptualization: Yoo-Jun Kim, Kiyoshi Tanaka, Hyodae Seo
Data curation: Yoo-Jun Kim, Yoshimasa Matsumura
Formal analysis: Yoo-Jun Kim
Funding acquisition: Yoo-Jun Kim, Kiyoshi Tanaka, Hyodae Seo, Yoshimasa Matsumura
Investigation: Yoo-Jun Kim, Kiyoshi Tanaka, Kosei Komatsu

The Role of Time- and Spatially Varying Wind in Coastal Circulation Based on High-Resolution Oceanic and Atmospheric Simulations

Yoo-Jun Kim[1], Kiyoshi Tanaka[1], Hyodae Seo[2], Kosei Komatsu[1], Yoshimasa Matsumura[3], César Sauvage[2], and Christoph Renkl[4]

[1]Atmosphere and Ocean Research Institute, The University of Tokyo, Kashiwa, Japan, [2]University of Hawai'i at Mānoa, Honolulu, HI, USA, [3]National Institute for Environmental Studies, Ibaraki, Japan, [4]University of Bonn, Bonn, Germany

Abstract Wind forcing plays a central role in oceanic circulation, including circulation in small bays where complex coastal orography modulates local winds both in time and space. However, their role in the circulation of such bays remains unclear because local winds are difficult to observe directly over the sea. Here, we used oceanic and atmospheric simulations with 100 m horizontal grid spacing, together with observations, to investigate wind-driven circulation under time- and spatially varying wind forcing in Otsuchi Bay. The simulation forced by time- and spatially varying winds reproduced the observed SSS distribution more closely than the simulation forced by time-varying but spatially uniform wind, which is a common simplification in coastal oceanic simulations. This improvement was explained by bay interior upwelling away from the coastline, which was not evident under spatially uniform wind forcing. This upwelling was driven by wind stress divergence rather than by wind stress curl. Spectral analysis showed that the relative importance of two mechanisms varied across timescales. Divergence-driven vertical motion was strongest at periods shorter than the local inertial period, but it became relatively weaker than curl-driven motion at longer periods. This study demonstrates that short-timescale wind stress divergence can drive bay interior upwelling and modify the SSS distribution in small bays. This finding further suggests that upwelling in small bays is not limited to coastline-confined upwelling or curl-driven Ekman upwelling. Accounting for divergence-driven upwelling is therefore important for understanding and modeling coastal circulation in small bays, with potential implications for the vertical transport of biogeochemical materials.

Plain Language Summary Wind drives oceanic currents. Local winds can vary from place to place and from hour to hour in small bays surrounded by complex coastal landforms, such as headlands and valleys. These local winds are difficult to observe over the sea, so their effects on oceanic circulation remain unclear. In this study, we used oceanic and atmospheric simulations together with observations to examine how winds that vary in time and space affect circulation in Otsuchi Bay. The oceanic simulation reproduced the observed surface salinity pattern better when local winds varied in both time and space than when only time-varying, spatially uniform winds were used, which is a common simplification in coastal oceanic simulations. This improvement was mainly caused by upwelling in the middle of the bay. The upwelling was driven by short-timescale wind stress divergence, rather than by wind stress curl. The results show that upwelling in small bays does not occur only along the coastline or through wind stress curl. It can also occur in the middle of the bay through wind stress divergence when local winds vary strongly in space and time. This process may also influence the vertical transport of nutrients and other materials in coastal waters.

1. Introduction

Oceanic circulation in narrow estuaries and small bays has been studied extensively worldwide. In such systems, where riverine water flows into the inner bay and eventually drains into the open ocean, surface currents are strongly influenced by local winds over the sea. Outside equatorial regions, these wind-driven surface currents are also subject to Earth's rotation, to some extent. These characteristics are common to many narrow estuaries and small bays across a wide range of geographical settings.

Classical studies have examined estuarine circulation in narrow estuaries and small bays using an idealized framework that assumes steady, horizontally uniform flow without rotation (e.g., Hansen & Rattray, 1965; Officer, 1976). Within this framework, these studies demonstrated that the surface component of density-driven

Methodology: Yoo-Jun Kim, Kiyoshi Tanaka, Hyodae Seo
Project administration: Kiyoshi Tanaka
Software: Yoo-Jun Kim, Yoshimasa Matsumura, César Sauvage, Christoph Renkl
Supervision: Kiyoshi Tanaka, Hyodae Seo
Validation: Yoo-Jun Kim
Visualization: Yoo-Jun Kim
Writing – original draft: Yoo-Jun Kim, Kiyoshi Tanaka, Hyodae Seo
Writing – review & editing: Yoo-Jun Kim, Kiyoshi Tanaka, Hyodae Seo, Kosei Komatsu, Yoshimasa Matsumura, César Sauvage, Christoph Renkl

circulation associated with riverine inflow can be strengthened or weakened depending on whether the local wind direction is aligned with or opposed to the surface current. Subsequent observational studies in such systems, including those in Chesapeake Bay (Wang, 1979), the Potomac River (Elliott, 1978), the Child River (Geyer, 1997), the York River (Scully et al., 2005), and Mobile Bay (Coogan & Dzwonkowski, 2018), provide strong support for this conceptual framework.

The idealized framework has been extended to examine how surface currents respond to time-varying local winds. Studies in Alberni Inlet (Farmer & Osborn, 1976), the Chilean fjords (Cáceres et al., 2002), Alfacs Bay (Llebot et al., 2014), and the Ría de Vigo (Gilcoto et al., 2017) have shown that surface currents respond to rapidly varying local wind forcing by aligning their direction with the wind direction within a few hours (e.g., about 1 hr in the Ría de Vigo). These observations indicate that, when wind direction and speed vary on timescales much shorter than the local inertial period, surface currents are directly pulled by the local wind, while the influence of Earth's rotation is secondary. Accordingly, under these conditions, surface currents do not approach a steady state but instead evolve continuously in time, responding to the local time-varying wind forcing. This highlights the importance of short-timescale wind variability in driving transient flow dynamics, referred to as the oceanic adjustment process, in fully understanding wind-driven circulation in coastal systems.

The role of spatially varying winds has also been investigated in studies of estuaries and fjords, including Jøsenfjord (Svendsen & Thompson, 1978), Porsangerfjorden (Myksvoll et al., 2012), the Patagonian Channels (Soto-Riquelme et al., 2023), and the Pearl River Estuary (Lai & Gan, 2023). These studies demonstrated that small-scale coastal orographic features surrounding narrow estuaries and small bays, such as coastal promontories, ridges, valleys, and nearby mountains, can generate pronounced spatial variability in the wind field, which in turn influences coastal circulation and associated material transport. These findings suggest that representing orographically induced wind variability in surface wind fields is important for understanding coastal circulation.

Moreover, the effect of Earth's rotation becomes important when the timescale of wind forcing exceeds the local inertial period. Although the Coriolis effect may be limited in narrow estuaries and small bays, it can still influence circulation under certain conditions. For instance, wind forcing that persists for a period longer than the inertial period, particularly when aligned with the bay axis, can drive a transverse flow across the bay through Ekman dynamics, thereby substantially modifying circulation patterns, as reported for Chesapeake Bay (Li & Li, 2012; Xie et al., 2017). Similarly, persistent wind stress curl generated by spatially varying winds can drive Ekman upwelling, as found in Suruga Bay (Tanaka et al., 2008) and Funka Bay (Takahashi et al., 2010).

Wind forcing is closely related to vertical circulation, which plays a crucial role not only in the dynamics of the circulation, but also in the vertical transport of nutrients and other biogeochemical tracers (e.g., Largier, 2020; Simpson & Sharples, 2012). Following Gill (1982), the vertical velocity directly induced by local winds at the sea surface can be expressed as:

$$\frac{\partial^2 w}{\partial t^2} + f^2 w = \frac{1}{\rho}\frac{\partial}{\partial t}\left(\frac{\partial \tau_x}{\partial x} + \frac{\partial \tau_y}{\partial y}\right) + \frac{f}{\rho}\left(\frac{\partial \tau_y}{\partial x} - \frac{\partial \tau_x}{\partial y}\right), \tag{1}$$

where w represents the vertical component of water velocity, x and y are horizontal Cartesian coordinates, and t denotes time. The surface wind stress is represented by τ_x and τ_y for the horizontal components in respective directions, and the Coriolis parameter and seawater density are denoted by f and ρ, respectively. The effects of horizontal advection, pressure gradient and viscosity are neglected. It should be noted that this equation explicitly includes the effects of time-varying local winds, spatially varying local winds, and Earth's rotation. When the wind forcing varies slowly on timescales much longer than the inertial period, the resulting oceanic motion is steady or quasi-steady, such that the second terms on the left- and right-hand sides balance each other, leading to the familiar Ekman upwelling/downwelling driven by wind stress curl. In contrast, when the wind forcing varies rapidly on timescales much shorter than the inertial period, the oceanic response is transient, reflecting an oceanic adjustment process, with the first terms on both sides balancing each other, indicating that the time-varying and divergence/convergence components of local wind stress cannot be neglected.

In the present study, we retain all terms in Equation 1 to examine wind-driven vertical motion induced by local winds that vary both in time and space under the influence of Earth's rotation in a small bay. This choice allows us to evaluate the relative roles of wind stress divergence and wind stress curl across timescales, rather than focusing on either process alone. Previous studies conducted in idealized settings have provided important motivation and physical insight into how wind stress divergence and wind stress curl influence oceanic responses. For example, using a two-layer model, Endoh (1971) examined the oceanic response to a traveling atmospheric disturbance that produces both wind stress divergence and wind stress curl over the open ocean. Similarly, Orlić and Pasarić (2011) derived an analytical solution for pycnocline oscillations at a coastal boundary, where the wind stress exhibits a discontinuity, using a reduced-gravity model. However, their relative roles in wind-driven vertical motion across timescales remain less clear in small bays where local winds are strongly shaped by coastal orography and vary in both time and space.

Building on these previous insights, the present study addresses the following questions for wind-driven circulation in a small bay surrounded by coastal orographic features. First, how do wind stress divergence and wind stress curl contribute to wind-driven vertical motion? Second, how does their relative importance vary across timescales from hourly to several days, spanning periods shorter and longer than the local inertial period? Third, what are the resulting impacts on bay interior upwelling and the sea surface salinity distribution associated with the river plume? As noted by Gill (1982), solving Equation 1 analytically is difficult, and we therefore address these questions using high-spatiotemporal resolution numerical simulations.

We focus on Otsuchi Bay on the east coast of Japan, a small bay surrounded by complex coastal orography (Figure 1). This study combines numerical simulations with observations in Otsuchi Bay. Multi-nested atmospheric simulations are conducted with progressively finer horizontal resolution down to 100 m, and the resulting winds are then used to force oceanic simulations with the same horizontal resolution. This approach is motivated by the hypothesis that time- and spatially varying wind fields affect bay interior upwelling and the sea surface salinity distribution in narrow estuaries and small bays, yet such wind data are rarely available from observations or reanalysis products. These simulations and observations provide a first step toward understanding wind-driven vertical circulation within an integrated land–air–sea system characterized by complex coastal orography.

2. Materials and Methods

2.1. Study Area

Otsuchi Bay is a semi-enclosed bay that extends several kilometers and opens eastward to the western North Pacific, while being bounded to the south, west, and north by coastal promontories, ridges, valleys, and nearby mountains (Figure 1c). This setting provides a useful case for examining wind-driven circulation in a small bay surrounded by coastal orography, because surface winds exhibit pronounced spatial and temporal variability. The internal Rossby radius of deformation of the river plume is also comparable to or smaller than the bay width of about 2 km, suggesting that rotational effects may be relevant to some degree in the bay. Otsuchi Bay is particularly well suited for this study because surface winds were observed at sea and land stations, allowing the simulated wind variability around the bay to be evaluated. Moreover, repeated high-spatial-resolution hydrographic observations were also available, providing an opportunity to evaluate simulated surface salinity distribution at scales of several hundred meters.

2.2. Observations

Shipboard surveys were conducted 15 times from June 2014 to November 2015, approximately once per month, using a Conductivity–Temperature–Depth (CTD) profiler (RINKO Profiler ASTD102, JFE Advantech). The spatial distribution of the 42 observation stations is shown in Figure 1c (black dots). The average distance between neighboring stations was approximately 400 m, and the surveys were generally completed in about 2 hr, with stations in the inner part of the bay completed within 1 hr.

Figure 2 shows a temperature-salinity diagram of sea surface water from all surveys. Due to inflows from rivers and the open ocean, sea surface salinity (SSS) exhibited greater variability among surveys than temperature. All surveys were used to estimate the spatial correlation structure required for the optimal interpolation described below. Among the 15 surveys, the survey conducted on 7 July 2015 (red squares in Figure 2) was selected for the detailed model-observation comparison because it captured a broad SSS range (29.2–33.2 psu) associated with riverine water, while the influence of high-salinity outer Pacific water was relatively limited. This condition made the July 7 survey suitable for evaluating how the simulated SSS structure responds to time- and spatially varying local winds.

10.1029/2026JC024033

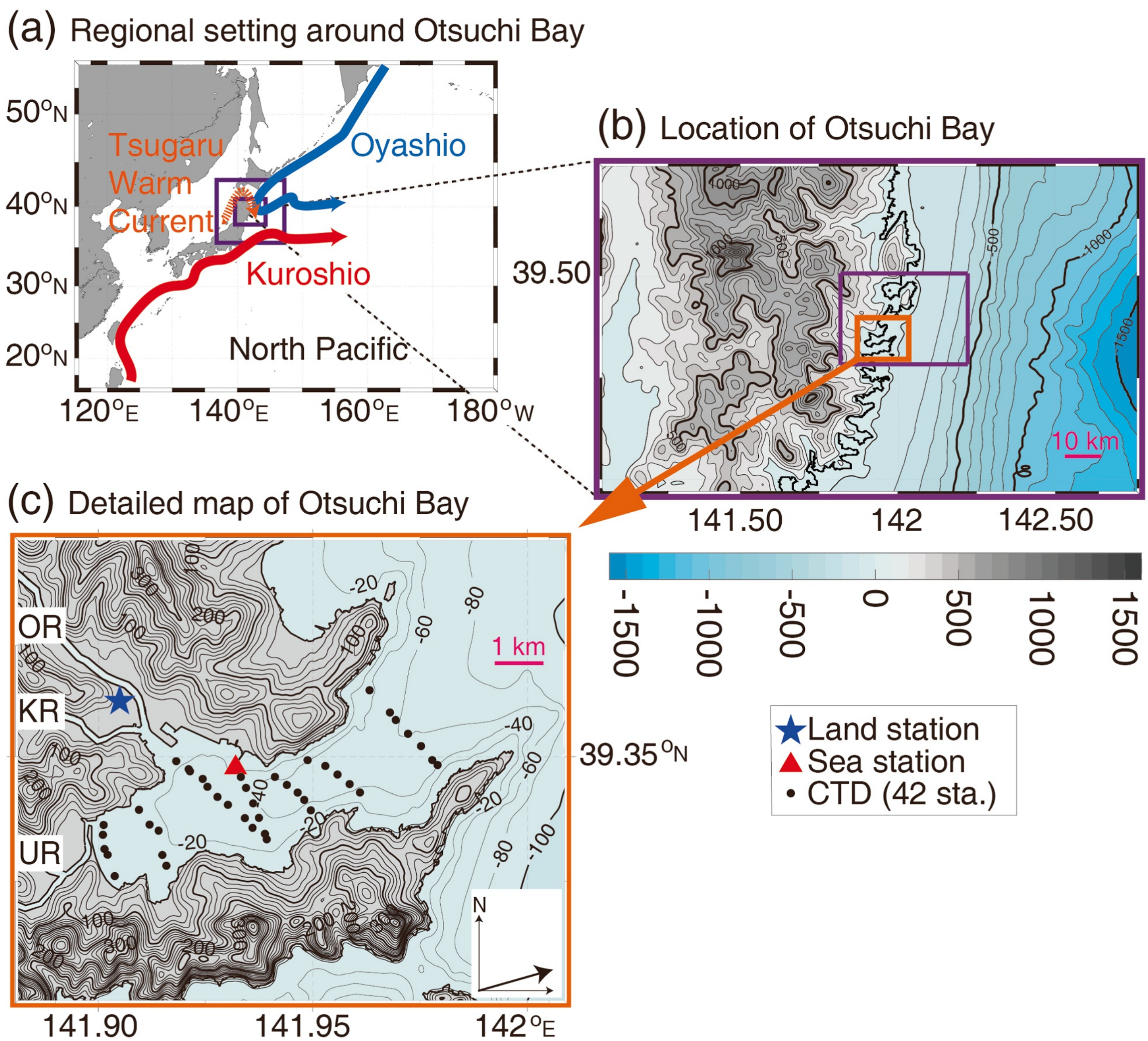

Figure 1. (a) Regional setting around Otsuchi Bay. Red, blue, and orange pathways indicate the Kuroshio, Oyashio, and Tsugaru Warm currents, respectively. Purple squares indicate domains of atmospheric simulations, D1 (outer) and D2 (inner). (b) Enlarged view showing the location of Otsuchi Bay. Purple squares indicate domains of atmospheric simulations, D3 (outer) and D4 (inner). (c) Detailed map of Otsuchi Bay. Black dots, the red triangle, and the blue star indicate CTD stations, wind measurements at sea station, and wind/precipitation measurements at land station, respectively. Contours represent coastal orography and bathymetry surrounding Otsuchi Bay. OR, KR, and UR denote the Otsuchi, Kozuchi, and Unosumai Rivers, respectively. The thick black arrow indicates the along-bay axis.

Wind over the sea was observed every 10 min using an anemometer (University of Tokyo) located in the middle of Otsuchi Bay (hereafter, the sea station; red triangle in Figure 1c). Wind velocity measured at a height of 7 m was converted to the value at 10 m using the conversion relation proposed by Johnson (1999).

Wind over the land was also observed every 10 min at a weather station (Japan Meteorological Agency; hereafter, the land station; blue star in Figure 1c). Similarly, wind velocity measured at a height of 5.5 m was converted to the value at 10 m. Precipitation data were also obtained at the same station to estimate river water flux.

2.3. Simulation of Sea Surface Wind

The Advanced Research version of the Weather Research and Forecasting (WRF) model (Skamarock et al., 2021) was used to simulate sea surface winds through multi-nesting, one-way dynamic downscaling. The one-way nested system consisted of four domains, with horizontal resolutions progressively increasing from 5,000 m in

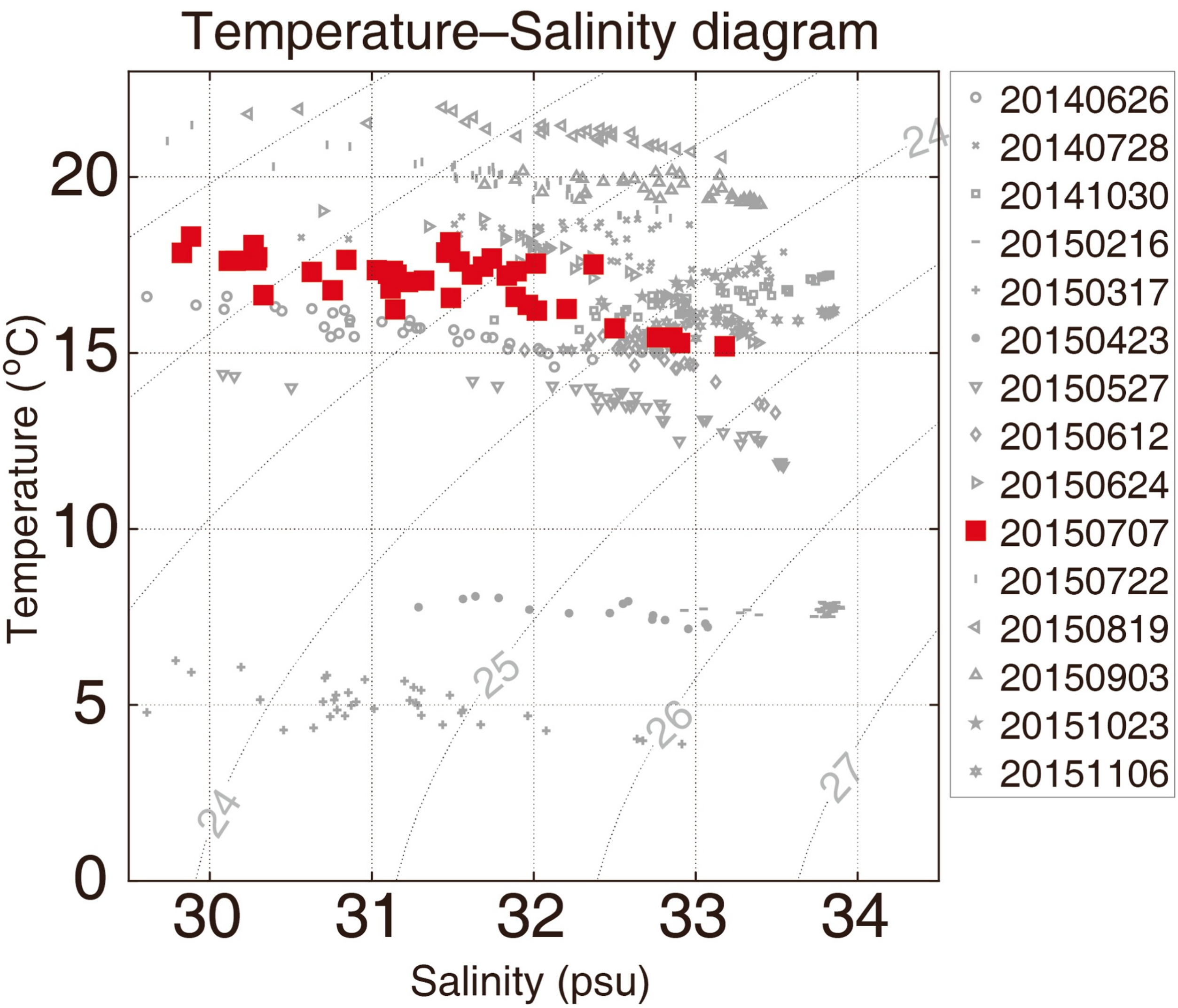

Figure 2. Temperature–Salinity diagram of observed surface seawater (averaged over 0–2 m depth).

the outermost domain (called D1) to 2,500 m in D2, 500 m in D3, and finally 100 m in the innermost domain (D4). Correspondingly, the model timestep decreased from 10 s to 2 s, 1 s, and 0.2 s, respectively. Each domain is shown by purple boxes in Figures 1a and 1b. All domains were configured with identical 40 vertical levels, and the thickness of the first layer above the surface was set to approximately 15 m.

Three-dimensional initial conditions for all domains and lateral boundary conditions for D1 were generated using ERA5 atmospheric global reanalysis data (Hersbach et al., 2020). The Mellor–Yamada–Nakanishi–Niino Level 3 (Nakanishi & Niino, 2006) planetary boundary layer scheme was applied to D1 and D2, while a three-dimensional LES scheme (Zhang et al., 2018) was applied to D3 and D4. Orographic features, such as coastal promontories, ridges, valleys, and nearby mountains in D4 (100 m resolution domain) were generated using 1 arc-second (~30 m) satellite altimetry data from the ALOS Global Digital Surface Model (AW3D30) provided by the Japan Aerospace Exploration Agency. Based on this orographic data, the land–sea mask (coastline) in D4 was also modified so that the bay was treated as oceanic grid points. The simulation period spanned more than 14 days, from June 23 to the morning of 7 July 2015, when the shipboard survey was conducted.

2.4. Simulation of Oceanic Circulation

KINACO, a non-hydrostatic, free-surface, z-level vertical coordinate ocean model (Matsumura & Hasumi, 2008) was used to simulate regional oceanic circulation. The simulation domain is shown in Figure 3a, with a horizontal

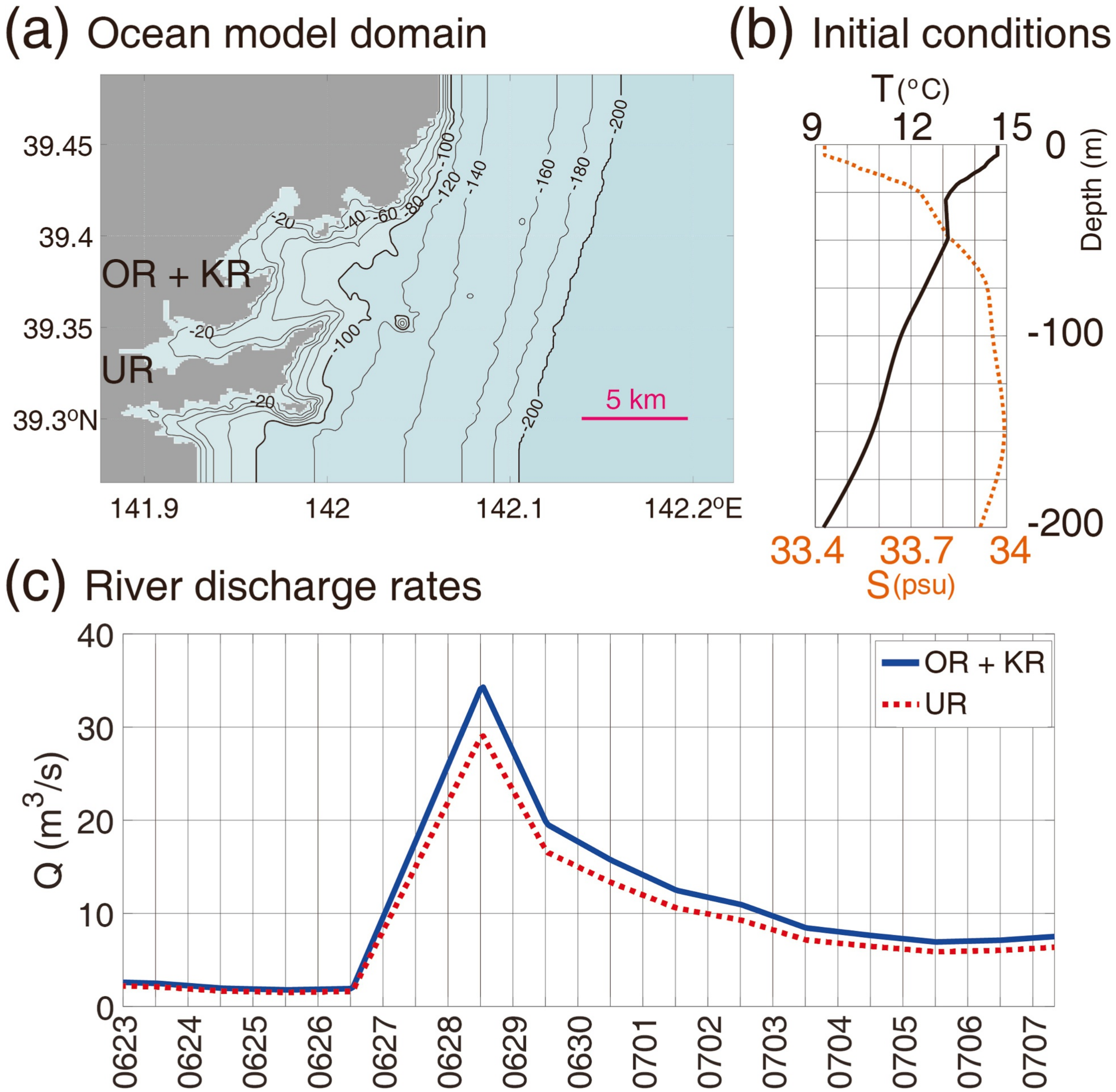

Figure 3. (a) Ocean model domain. (b) Initial conditions of temperature (T, black solid line) and salinity (S, orange dashed line). (c) River discharge rates. Freshwater fluxes were applied to the river area in (a).

resolution of 100 m. The horizontal grid points were matched with those of the 100 m atmospheric simulation (D4) to prevent grid-mismatch-induced errors. In the vertical direction, 80 levels were configured, with a resolution of 1 m in the uppermost layer (0–20 m), gradually increasing to 4 m in the lowermost layer, reaching a maximum depth of 200 m, while the timestep was 2 s. The simulation period was identical to that of the atmospheric simulations.

The bathymetry was generated using the data set used by Sakamoto et al. (2017). The initial conditions of temperature and salinity were provided by the profiles shown in Figure 3b. The upper part of the profiles was derived from our shipboard survey on July 7, while the lower part was derived from the Offshore Fixed Line Oceanographic Observation Results in July 2015, provided by the Iwate Fisheries Technology Center. The initial conditions were set to be horizontally uniform, a common approach in local bay simulations when realistic near-coastal hydrographic fields are unavailable from coarse-resolution reanalysis or larger-scale model products (e.g., Sakamoto et al., 2017; Tanaka et al., 2008). The Smagorinsky-type lateral mixing (Smagorinsky, 1963) was applied with a constant of 0.1, and the generic length scale vertical mixing parameterization (Umlauf & Burchard, 2003) was applied with a background value of 1×10^{-6} m^2 s^{-1}. At the surface boundary, wind stress was imposed without heat fluxes, evaporation, or precipitation to focus on momentum transfer induced by time- and spatially varying winds. Additional sensitivity experiments with heat fluxes or alternative wind forcing are summarized in the Supporting Information S1.

River inflow was prescribed as freshwater fluxes applied at the surface of innermost grid cells at the mouths of the Otsuchi/Kozuchi and Unosumai Rivers (Figure 3a). Freshwater fluxes during the simulation period were estimated using empirical discharge models derived from daily river discharge observations and precipitation records from 2011 to 2013. In these models, river discharge was represented as a linear combination of precipitation data over the preceding days. Specifically, the coefficients of the empirical models were obtained by fitting the observed daily river discharge to the preceding 30 days of precipitation records during 2011–2013. The resulting coefficients were then applied to the corresponding precipitation data during the simulation period to estimate freshwater fluxes. Separate models were constructed for each river. Estimated freshwater fluxes for the simulation period are shown in Figure 3c.

At the lateral boundaries, hourly barotropic tidal velocities were imposed using the Flather condition (Flather, 1976), which adjusts the normal velocities with respect to the prescribed sea surface height. The barotropic tidal velocities and sea surface heights were adopted from the TPXO tide model (Egbert & Erofeeva, 2002). Temperature and salinity, together with other baroclinic properties were subject to radiation conditions using zero-gradient conditions (Carter & Merrifield, 2007) with a sponge layer to damp reflections. In addition, temperature and salinity were weakly restored to the reference profiles shown in Figure 3b with a daily timescale to relax isopycnal displacement (e.g., Carter & Merrifield, 2007).

3. Results

3.1. Observed Sea Surface Salinity Distribution on July 7, 2015

The distribution of sea surface salinity (SSS) on 7 July 2015 was mapped using an optimal interpolation method. In this method, interpolation weights are determined by a prescribed correlation function that relates an estimate at a given location to surrounding observations. Classical implementations (e.g., Brasseur et al., 1996) construct the correlation function by fitting correlations between observation stations to their separation distance, assuming that correlations decrease uniformly with distance and are independent of direction (isotropic).

This assumption is sometimes difficult to apply in coastal regions, where correlations can be influenced by geographic constraints such as bay geometry. This was also the case in Otsuchi Bay. Correlations between observation stations, estimated from our 15 surveyed SSS data sets, were higher in the along-bay direction than in the cross-bay direction (figure not shown). This directional dependence likely reflects circulation constrained by the elongated shape of the bay and suggests that an isotropic correlation function may not be appropriate for mapping SSS in this region.

In addition, SSS in Otsuchi Bay is influenced not only by riverine freshwater but also by outer Pacific waters, including seasonal variations associated with Oyashio water and Tsugaru Warm Current water, which have salinity ranges of 33–33.7 psu and 33.7–34.2 psu, respectively (Hanawa & Mitsudera, 1986). To better characterize the inner-bay SSS structure associated with low-salinity riverine water, we reduced the influence of offshore Pacific water when estimating correlations between stations. This preprocessing was applied because offshore water intrusion can introduce a bay-wide coherent salinity signal, which may obscure the spatial correlation structure associated with low-salinity riverine water. Previous studies have shown that Pacific water intrudes into Otsuchi Bay primarily along the northern coast (Otobe et al., 2009; see also Ishizu et al., 2017; Tanaka et al., 2017). Accordingly, for each survey, the SSS value observed at the northern outermost station was assumed to represent the Pacific water component and was subtracted from observed SSS values at all other stations. Correlations between observation stations were then estimated using these residual SSS values.

Based on the directional dependence identified in the correlations between observation stations, a direction-dependent (i.e., anisotropic) correlation function (μ) was adopted for the optimal interpolation method. The formulation follows Kuragano and Kamachi (2000) with minor modifications and is expressed as:

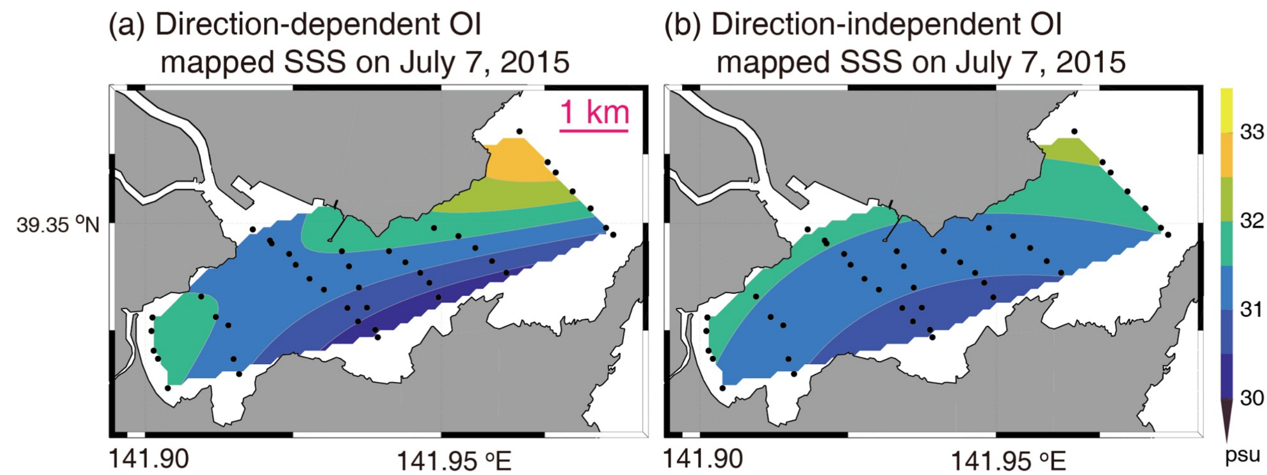

Figure 4. Observed SSS distribution on 7 July 2015, (a) mapped using the direction-dependent (anisotropic) and (b) mapped using direction-independent optimal interpolation methods.

$$\mu(\Delta x, \Delta y) = \exp\left(a_1\ \Delta x^2 + a_2\ \Delta y^2 + a_3\ \Delta x \Delta y + a_4\right), \quad (2)$$

where, Δx and Δy denote zonal and meridional distance, respectively. The coefficients a_1, a_2, a_3, and a_4 were obtained through curve-fitting (−0.0413, −0.2398, 0.1154, and −0.2324, respectively). The coefficients a_1, a_2, and a_3 control the anisotropic shape of the correlation function, which forms elliptical contours in the horizontal plane and defines the major and minor axes as well as the tilt angle of the ellipse. The coefficient a_4 represents a constant related to the signal-to-noise ratio. The substantial difference between a_1 (–0.0413) and a_2 (–0.2398) indicates pronounced anisotropy in the along- and cross-bay directions, supporting the use of an anisotropic correlation function for optimal interpolation in this bay.

Figures 4a and 4b show the SSS distribution mapped at high spatial resolution (less than 1 km) using the direction-dependent and direction-independent optimal interpolation methods, respectively. Notably, in Figure 4a, the lowest-salinity water did not appear near the river mouths but was instead distributed along the southern coast of the bay, forming a pronounced north–south salinity gradient away from the river mouths. In contrast, a small area of relatively high-salinity water appeared in the innermost part of the bay, near the Unosumai River (UR) mouth. It should be noted that these features were more strongly smoothed in the direction-independent optimal interpolation result (Figure 4b). The correlation with the observed SSS values at the stations was also lower for the direction-independent result (0.72) than for the direction-dependent result (0.84). Together, these differences indicate the importance of using a correlation function that accounts for directional dependence. Repeated observations allowed this directional dependence of spatial correlations to be estimated more reliably than from a single survey.

3.2. Simulated Sea Surface Wind

Figure 5 shows representative examples of the simulated surface wind vectors and wind stress divergence in D4, the innermost domain with 100 m resolution, during the sea breeze period at 12:00 local time on 6 July in Figure 5a, the land breeze period at 05:00 local time on 7 July in Figure 5b, and the mean field over the simulation period in Figure 5c. Wind stress, $\tau(\tau_x, \tau_y)$ was estimated using a bulk formula, $\tau = \rho_A C_d \mathbb{U}|\mathbb{U}|$, where ρ_A is air density (1.225 kg m^{-3}), C_d is the drag coefficient (0.0015), and $\mathbb{U}(U_{10}, V_{10})$ represents the wind velocity at 10 m height. During the daytime (Figure 5a), easterly (landward) winds were dominant, whereas at night (Figure 5b), westerly (offshore) winds were dominant. Compared with the weaker mean wind field shown in Figure 5c, this contrast between the daytime and nighttime wind fields indicates pronounced temporal variability over the bay on timescales of a day or less.

During both the sea and land breeze periods, wind speed and direction were strongly modulated by coastal orographic features, including coastal promontories, ridges, valleys, and nearby mountains, resulting in numerous

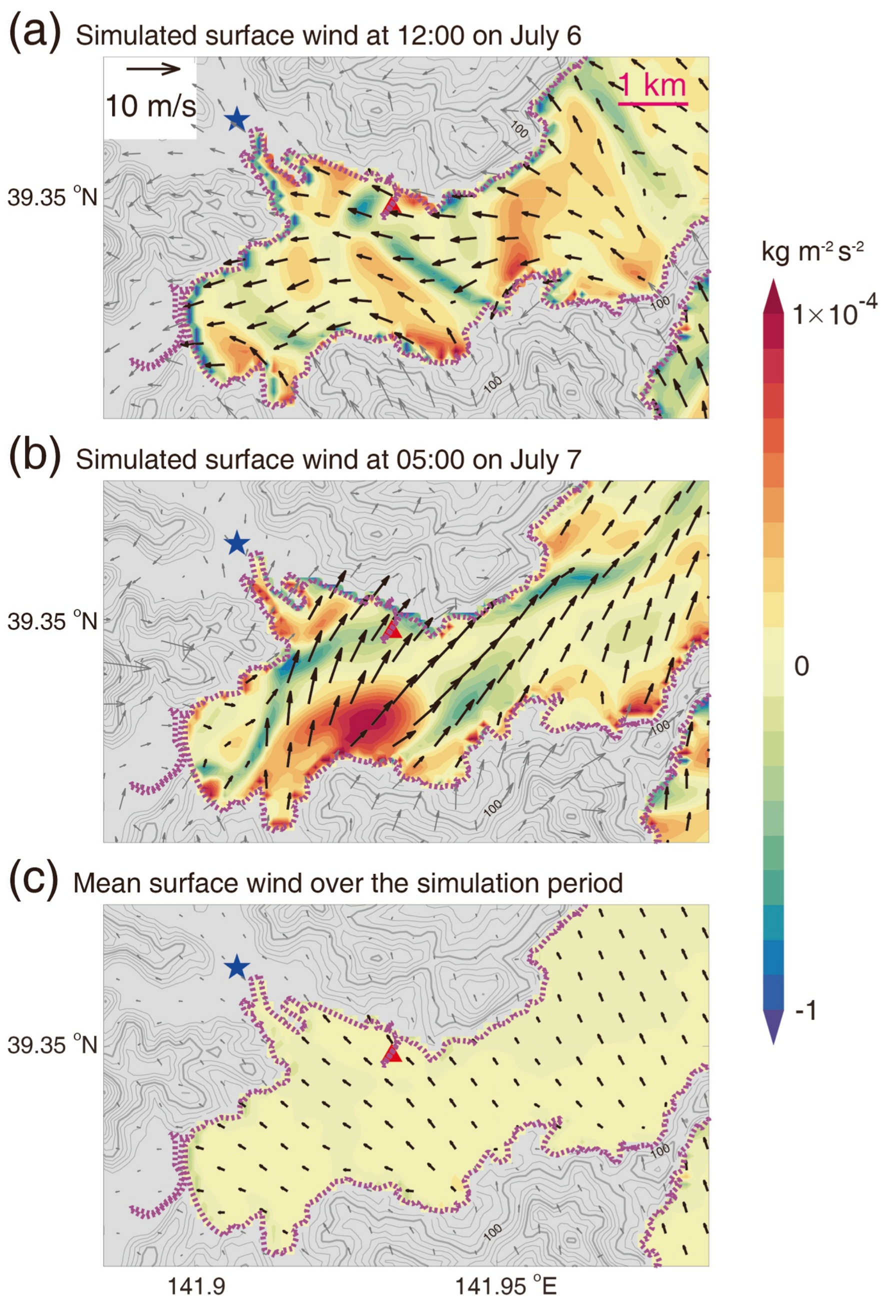

Figure 5. Representative examples of the simulated surface wind vectors and wind stress divergence. (a) at 12:00 on July 6, (b) at 05:00 on July 7, local time, and (c) mean field over the simulation period. The color field shows wind stress divergence over the sea, with red indicating divergence and blue indicating convergence. Black and gray vectors indicate winds over the sea and land, respectively. The purple dashed line indicates the actual coastline.

small-scale wind structures over the bay. These small-scale wind structures, in turn, generated localized divergence/convergence of wind stress over the sea (color field in Figure 5). For example, during the land breeze period, a broad region of wind stress divergence developed in the southern inner part of the bay (reddish zone in Figure 5b), particularly in front of a coastal promontory, while surrounding areas were characterized by wind stress convergence (blueish zone).

The localized wind stress divergence/convergence structures differed between the wind fields shown in Figures 5a and 5b, despite the two fields being only 17 hr apart. This difference suggests that these small-scale structures can vary substantially within the local inertial period of 18.9 hr. These structures were much less

10.1029/2026JC024033

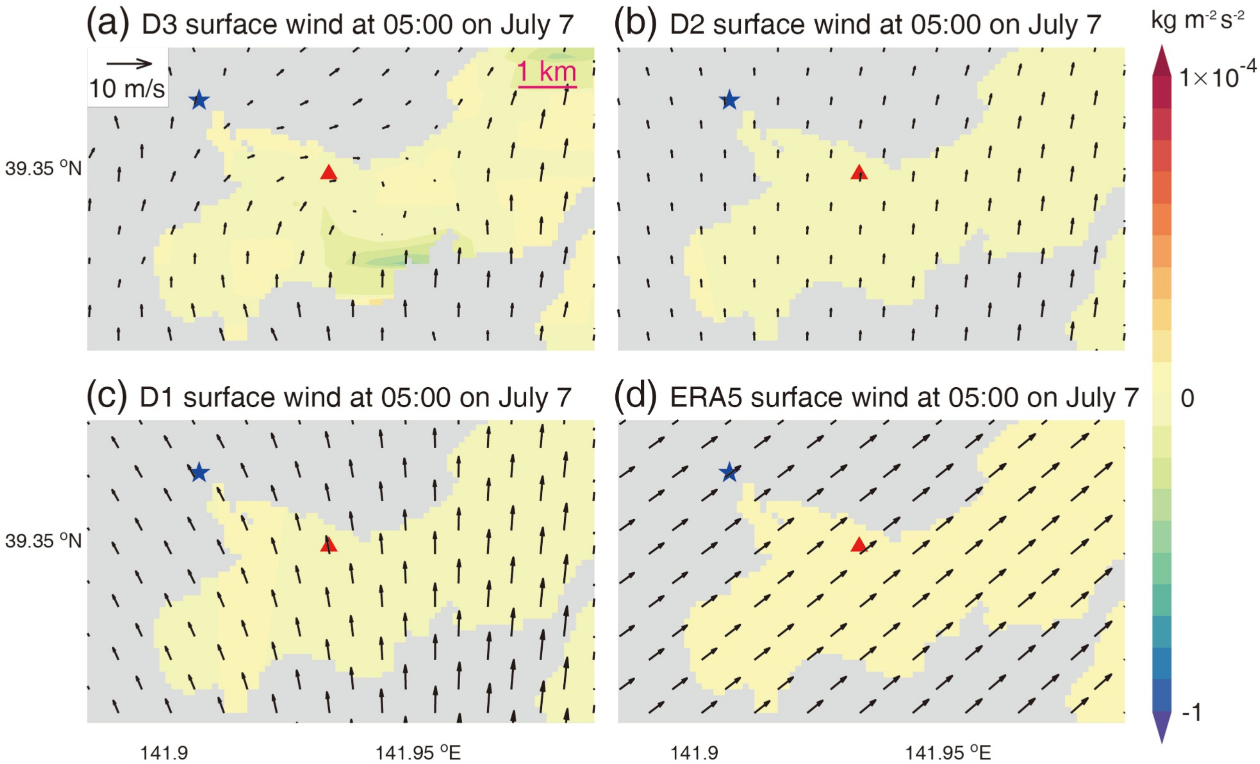

Figure 6. Same as Figure 5b but for (a) D3, (b) D2, (c) D1, and (d) ERA5 wind fields at 05:00 on July 7, local time. The color field shows wind stress divergence over the sea and gray shading indicates land mask in D4.

evident in the mean D4 wind field (Figure 5c) and were also less distinct in the coarser wind fields (Figure 6), indicating that they reflect both short-timescale variability and the small-scale spatial structure of local winds. Because these localized divergence/convergence structures are directly relevant to the bay interior response examined in the following sections, the D4 wind field was used in the subsequent oceanic simulations and analyses.

To assess whether simulated wind fields (D4) also reflect the observed wind variability at the two stations, Figures 7a and 7b compare the simulated and observed surface wind velocities at the sea and land stations, respectively. The simulated winds reproduced the observed temporal variability at both stations, although some differences in timing and amplitude were present. The correlations at the sea station were 0.69 and 0.70 for the zonal and meridional wind, respectively, and the corresponding root-mean-squared error (RMSE) values were 2.43 and 2.45 m s^{-1}. At the land station, the correlations were 0.76 and 0.71 for the zonal and meridional wind, respectively, and the corresponding RMSE values were 1.22 and 1.51 m s^{-1}. These RMSE values were comparable to the observed wind standard deviations of 2.61 and 3.02 m s^{-1} at the sea station and 1.61 and 1.92 m s^{-1} at the land station. Therefore, despite remaining discrepancies, especially at the sea station where sub-grid-scale orographic effects, including those associated with a nearby small island southwest of the station (Figure 1c), may locally influence the point wind observations, the simulated wind field is considered to reasonably represent the local wind conditions.

3.3. Simulated Sea Surface Salinity Distribution

Regional oceanic simulations with a 100 m horizontal grid spacing were conducted to examine how time- and spatially varying wind affected the simulated SSS distribution on 7 July 2015. Two cases of hourly wind forcing were imposed on the sea surface: Case_H, forced by the time- and spatially varying wind field from the atmospheric simulation (Section 3.2), and Case_U, forced by a time-varying but spatially uniform wind field. In Case_U, wind data at a single point, the sea station, in the same atmospheric simulation were uniformly applied across the entire domain. The use of spatially uniform wind forcing while retaining temporal variability from a

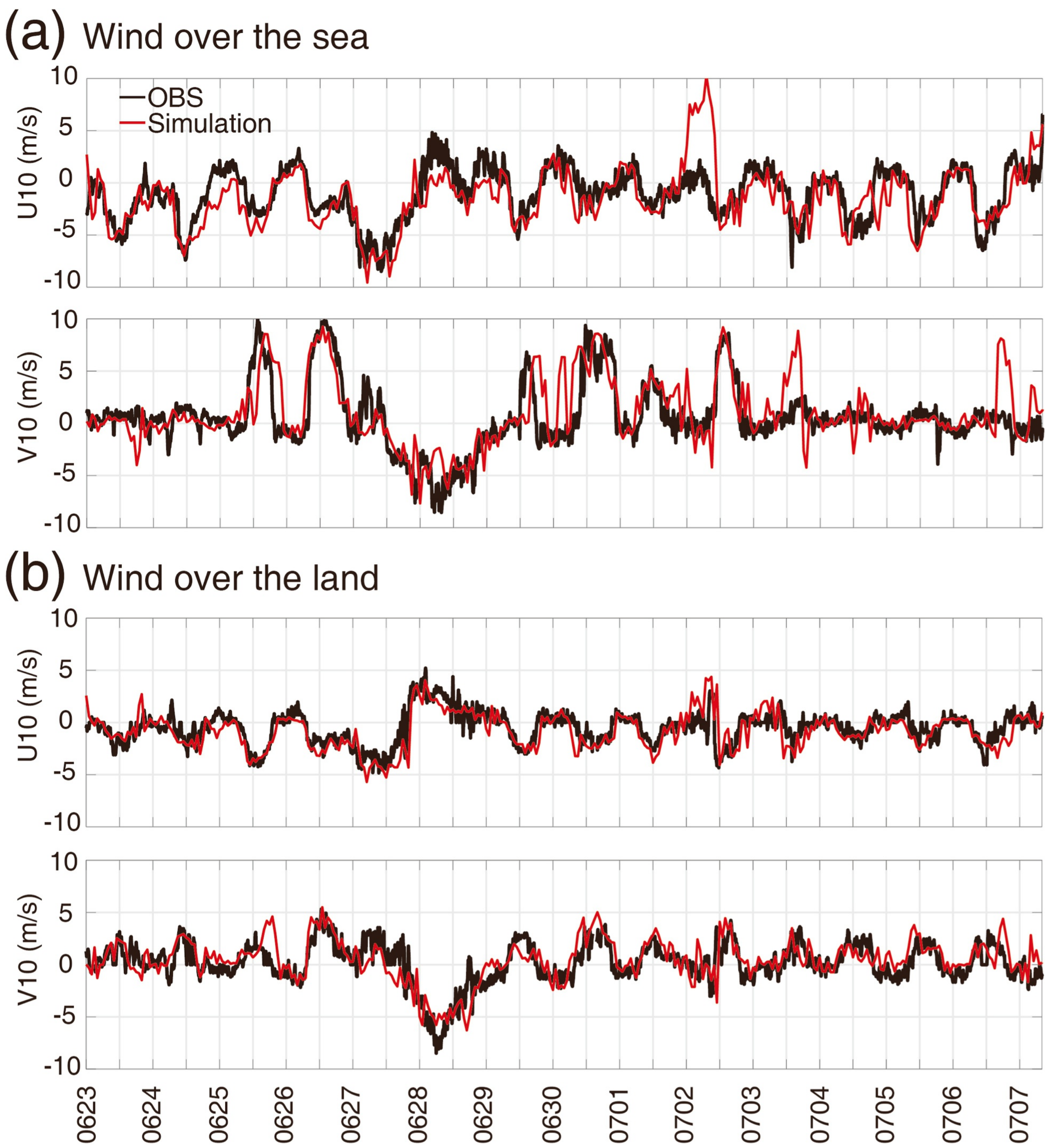

Figure 7. Wind at a height of 10 m, (a) at the sea station, and (b) at the land station. Black and red solid lines represent observed and simulated wind, respectively. Red solid lines were constructed with values spatially averaged over 3 × 3 grids surrounding the model grid point closest to each observation station to reduce high-frequency noise.

single-station wind record is a common practice in small-scale bay circulation modeling (e.g., Sakamoto et al., 2017).

Figures 8a and 8b show the simulated SSS distributions in Case_H and Case_U, respectively, at the start of the CTD survey (08:30 on 7 July local time), after more than 2 weeks of model integration. The distinctive features of the observed SSS distribution (Figure 4) are more closely reproduced in Case_H, including the presence of the lowest-salinity water along the southern coast away from the river mouths, the sharp north–south salinity

10.1029/2026JC024033

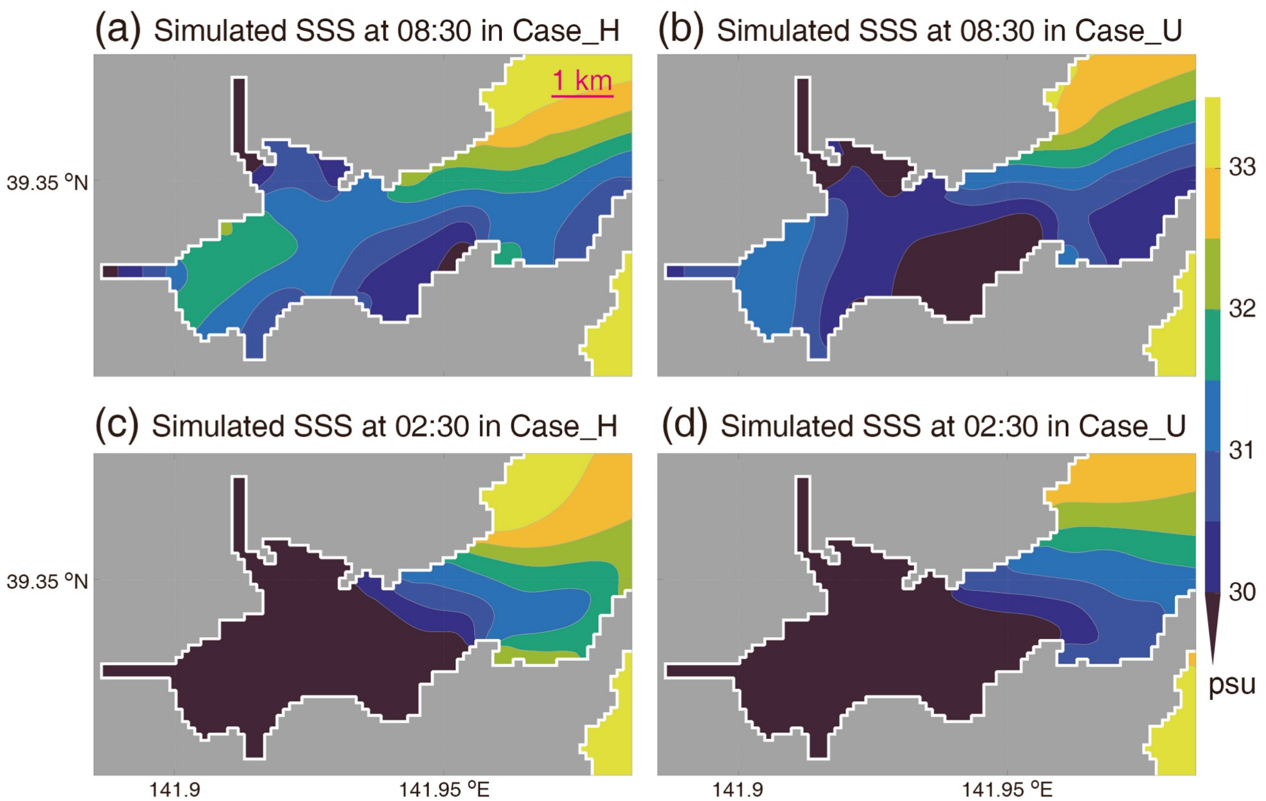

Figure 8. Simulated SSS distributions. (a) at 08:30 in Case_H, (b) at 08:30 in Case_U, (c) at 02:30 in Case_H, and (d) at 02:30 in Case_U on July 7, local time.

gradient, and the small region of relatively high-salinity water in the innermost part of the bay. In contrast, Case_U underestimates SSS over much of the bay, with salinity values lower than the observations by at least 0.5 psu, although the lowest-salinity water still appears along the southern coast.

The corresponding scatter plots against the observations are shown in Figure 9. These plots provide a compact summary of the differences seen in Figures 8a and 8b. Case_H shows a smaller RMSE and a near-zero bias (0.23 psu and −0.04 psu, respectively). In contrast, Case_U shows a substantially larger RMSE (0.85 psu) together with a larger negative bias (−0.79 psu), indicating a broad underestimation of SSS. This improved agreement in Case_H suggests that the influence of the remaining wind discrepancies, particularly those at the sea station, on the simulated SSS distribution was limited during the survey period. Compared with Case_H, the additional experimental cases using different wind forcings (D3, D2, D1, ERA5, and no-wind forcing) generally showed SSS patterns that were less consistent with the observations, whereas the heat-flux case showed almost no difference from Case_H (Figure S1 in Supporting Information S1).

At an earlier time (02:30 on 7 July local time), the two simulations showed similar distributions (Figures 8c and 8d), providing a useful baseline for examining the subsequent development of their differences. In both cases, riverine water with salinity below 30 psu covered most of the bay surface. The differences between the two distributions at 08:30 local time (Figures 8a and 8b) therefore developed over the subsequent 6 hr, as the two simulations responded to wind forcing with contrasting spatial structures. To identify the physical processes responsible for the development of these differences, a simplified surface-layer salt budget was examined. Following Feng et al. (1998), the surface-layer salt budget under conditions with no precipitation or evaporation is given by:

$$\frac{\partial \langle S \rangle}{\partial t} = -\frac{1}{d} S' w|_{-d} + \text{residual}, \tag{3}$$

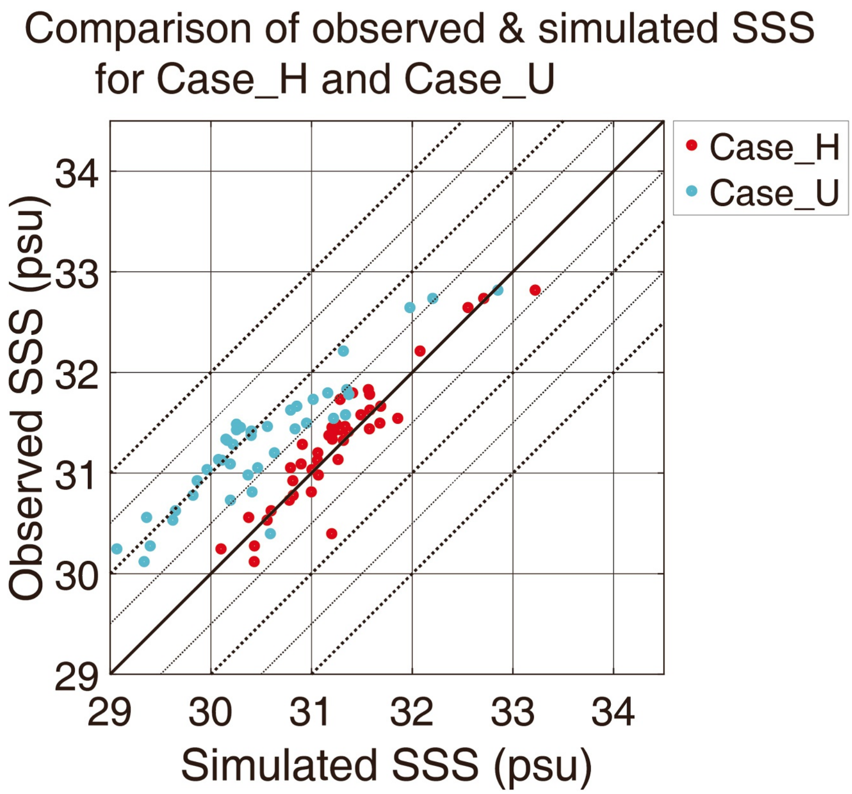

Figure 9. Scatter plots comparing observed and simulated SSS at the CTD stations at 08:30 on July 7, local time. Red and light blue denote Case_H and Case_U, respectively. The solid black line indicates the one-to-one line. Thin dashed lines indicate differences from the one-to-one line at 0.5 psu intervals.

where, $\langle S \rangle = \frac{1}{d}\int_{-d}^{\text{surface}} S\,dz$ denotes the vertically averaged salinity in the surface-layer, S' represents the salinity difference between $\langle S \rangle$ and the subsurface salinity at a depth d (=2 m), and $w|_{-d}$ denotes the vertical velocity at depth d. In the present simulations, surface heat fluxes, evaporation, or precipitation are not applied, and thus surface freshwater fluxes do not contribute to the budget. Horizontal advection, and mixing are included in the residual term, whose contribution is evaluated in the subsequent budget-difference analysis. Using Equation 3, the salinity tendency difference between two simulations can be expressed as:

$$\frac{\partial}{\partial t}(\langle S_H \rangle - \langle S_U \rangle) = -\frac{1}{d}\left[S'_H w_H|_{-d} - S'_U w_U|_{-d}\right] + \text{residual}, \tag{4}$$

where, subscripts H and U denote quantities from Case_H and Case_U, respectively. The right-hand side of Equation 4 can be further decomposed as:

$$\frac{\partial}{\partial \mathrm{t}}(\langle S_H \rangle - \langle S_U \rangle) = -\frac{1}{\mathrm{d}}\Big[S'_U\left(w_H|_{-\mathrm{d}} - w_U|_{-\mathrm{d}}\right) + (S'_H - S'_U)\,w_U|_{-\mathrm{d}} \\ + (S'_H - S'_U)\left(w_H|_{-\mathrm{d}} - w_U|_{-\mathrm{d}}\right)\Big] + \text{residual}, \tag{5}$$

where the first term represents the contribution from differences in vertical velocity, the second term represents the contribution from differences in vertical salinity structure, and the third term represents their interaction.

Figure 10 shows the time-integrated contributions of these terms from 02:30 to 08:30 local time. A pronounced positive salinity tendency appears in the central part of the bay (boxed region in Figure 10a), identifying the location and magnitude of the salinity increase in Case_H relative to Case_U during the 6-hr period, with an average increase of 0.67 psu. The decomposition results are shown in Figures 10b and 10c. The contribution associated with differences in vertical velocity dominates the salinity tendency difference (Figure 10b),

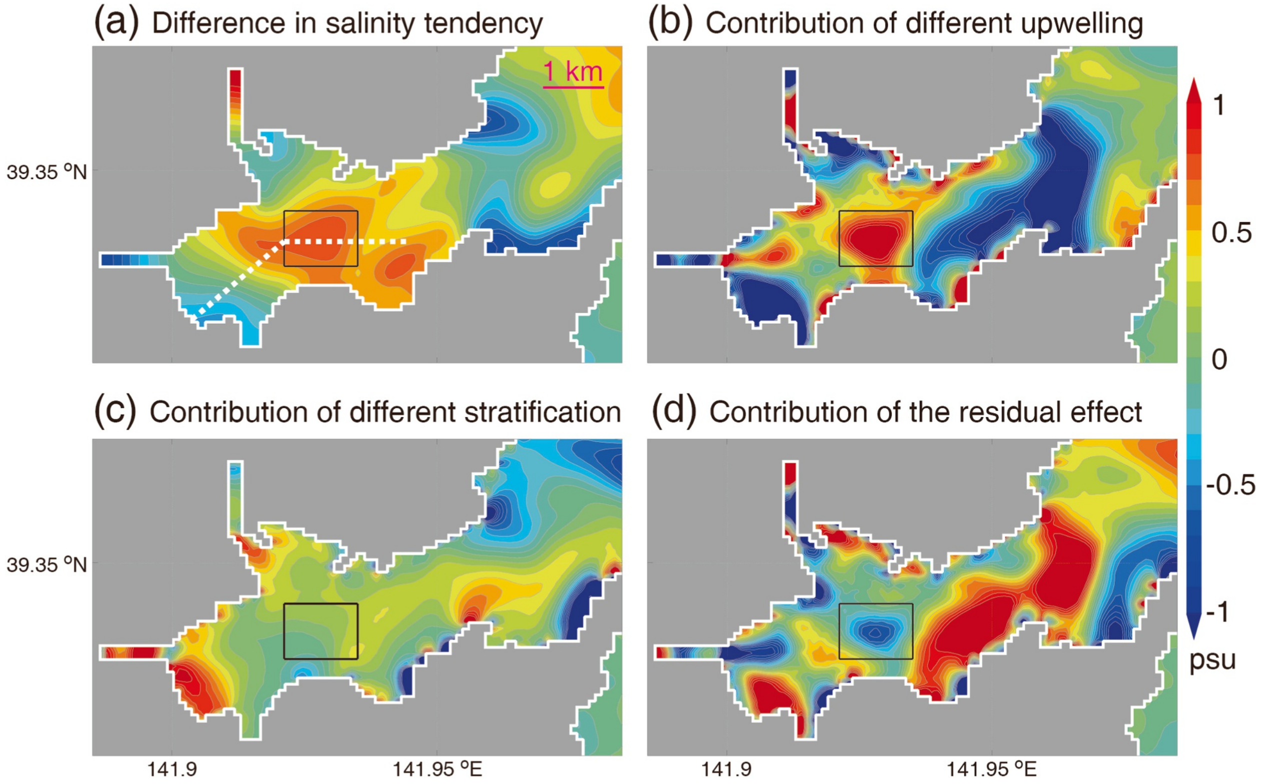

Figure 10. Time-integrated contributions of each term in surface-layer salt budget from 02:30 to 08:30 on July 7, local time (a) difference in salinity tendency, (b) contribution of different upwelling, (c) contribution of different stratification, and (d) contribution of the residual effect.

accounting for an increase of 0.73 psu within the boxed region. In contrast, differences in vertical salinity structure contribute only 0.11 psu (Figure 10c). The contribution from the interaction term is an order of magnitude smaller, at approximately 0.01 psu (figure not shown). Figure 10d shows that the residual term, which includes differences in horizontal advection and mixing, is negative in the boxed region and therefore does not contribute to the positive salinity tendency. These results indicate that stronger upwelling in the middle of the bay under spatially varying wind forcing was the primary mechanism responsible for the improved SSS representation in Case_H compared with Case_U. This finding highlights the importance of oceanic responses to small-scale wind structures over a short period for reproducing the observed salinity distribution.

The simulated vertical circulation provides a dynamically consistent interpretation of this salt-budget result. Figures 11a and 11b show the vertical circulation along the bay axis in Case_H and in Case_U. Vertical

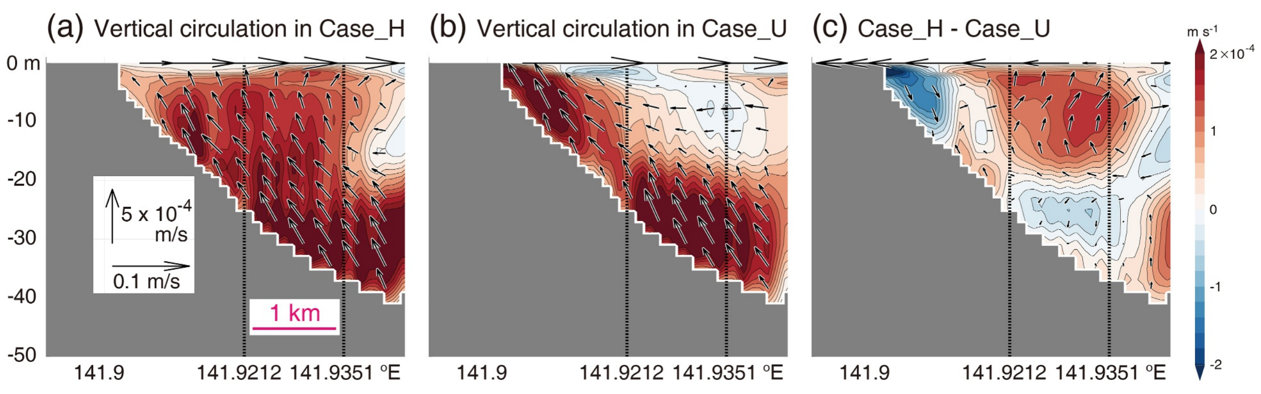

Figure 11. Vertical sections along the white dashed line in Figure 10a. (a) Case_H, (b) Case_U, and (c) difference between Case_H and Case_U. Vectors indicate flow velocity and direction, and color field represents vertical velocity.

circulation in Case_U exhibits a classical estuarine circulation pattern characterized by surface outflow and subsurface inflow, and upwelling confined to the coastline (e.g., Hansen & Rattray, 1965). Figure 11c shows the difference between Case_H and Case_U, revealing enhanced upwelling in the middle of the bay under spatially varying wind forcing. As a consequence of stronger upwelling in Case_H (Figure 10b), the vertical circulation becomes stronger between the dashed lines in Figure 11c, and this enhancement extends to a depth of approximately 20 m. These results suggest that spatially varying wind forcing can enable substantial vertical transport in the interior of the bay, away from the coastline, with potential implications for the vertical transport of tracers such as nutrients.

3.4. Role of Time- and Spatially Varying Wind Under the Influence of Earth's Rotation

Under time- and spatially varying wind forcing, Case_H showed enhanced upwelling in the interior of the bay, away from the coastline, together with improved consistency with the observed SSS distribution. In contrast, this bay interior upwelling was absent in Case_U, where spatially uniform wind forcing produced negligible wind stress curl and divergence. The dynamical mechanism responsible for the enhanced upwelling in the interior of the bay in Case_H is further examined using Equation 1, with a focus on how time- and spatially varying wind forcing drives the vertical motion under the influence of Earth's rotation.

Equation 1 indicates that vertical motion can be generated under spatially varying wind forcing through two distinct mechanisms: wind stress curl and wind stress divergence. These two mechanisms are associated with different characteristic timescales, governed by the Coriolis parameter (f) and the temporal derivative ($\partial/\partial t$), respectively, as discussed below.

When wind variability is much slower than the local inertial period, ($\partial/\partial t \ll f$), the balance in Equation 1 reduces to the curl-driven Ekman response. The curl-based estimate of vertical velocity (w_{curl}) is then given by

$$w_{\text{curl}} = \frac{1}{\rho f}\left(\frac{\partial \tau_y}{\partial x} - \frac{\partial \tau_x}{\partial y}\right), \tag{6}$$

where ρ (=1,025 kg m^{-3}) is the reference seawater density and f (=9.23×10^{-5} s^{-1}) is the Coriolis parameter at the latitude of Otsuchi Bay. Figure 12a shows the time-averaged curl-based vertical velocity from 02:30 to 08:30 local time. Despite the enhanced bay interior upwelling simulated in Case_H (Figure 10b within the boxed region and Figure 11c between the dashed lines), the curl-based estimate indicates downwelling and exhibits a spatial pattern inconsistent with the simulated response. This discrepancy arises because the spatially varying wind field during this period produces predominantly negative wind stress curl.

In contrast, when wind variability is much faster than the inertial period, ($\partial/\partial t \gg f$), vertical motion is governed by divergence-driven oceanic adjustment. The divergence-based estimate of vertical velocity (w_{div}) is given by:

$$\frac{\partial w_{\text{div}}}{\partial t} = \frac{1}{\rho}\left(\frac{\partial \tau_x}{\partial x} + \frac{\partial \tau_y}{\partial y}\right). \tag{7}$$

This estimate was obtained by integrating Equation 7 from 02:30 to 08:30 local time and then averaging over the same time-interval. As shown in Figure 12b, the divergence-based estimate closely matches both the magnitude and spatial structure of the enhanced bay interior upwelling simulated in Case_H (Figure 11c), reflecting the positive wind stress divergence generated by the spatially varying wind field (Figure 5b). Within the boxed region, this divergence-based estimate of vertical velocity implies an upward isopycnal displacement of approximately 1.86 m over the 6-hr period. Consistent with this estimate, the depth of the 1,025 kg m^{-3} isopycnal in Case_H shoaled from approximately 4 m to 2 m during this period. In contrast, the curl-based estimate predicts a much smaller vertical displacement of approximately 0.10 m, directed downward, which is an order of magnitude weaker than the divergence-induced displacement. These results indicate that the enhanced upwelling in the middle of the bay in Case_H is explained mainly by divergence-driven adjustment rather than by curl-driven Ekman dynamics.

These results can be interpreted through the associated timescale implied by Equation 1. Curl-driven Ekman response scales with the Coriolis parameter f, which represents the inertial period (i.e., dominant when $\partial/\partial t \ll f$), whereas divergence-driven adjustment response scales with temporal variability of the wind (i.e.,

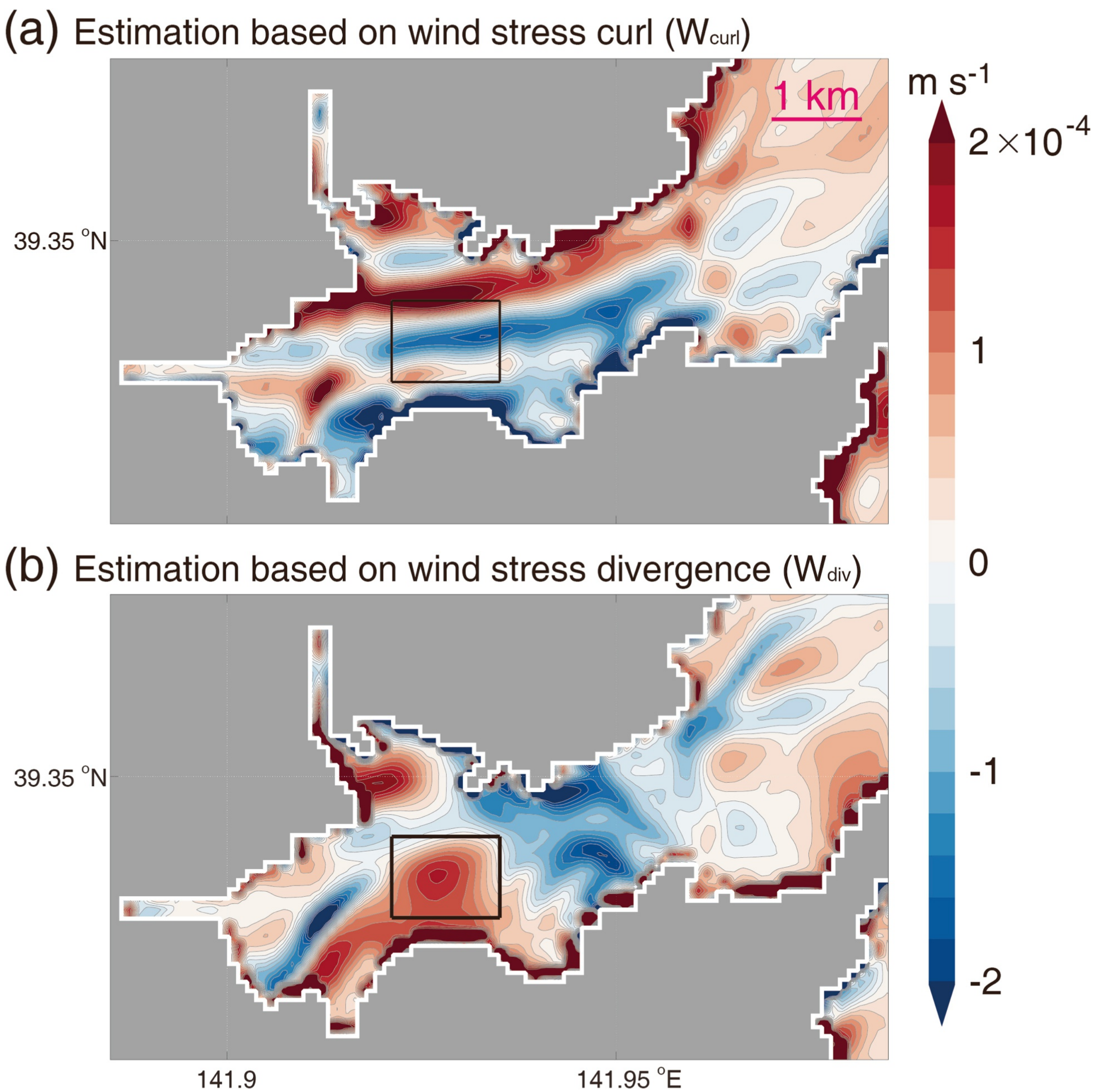

Figure 12. Estimated mean vertical velocity from 02:30 to 08:30 on July 7, local time. (a) curl-based estimation and (b) divergence-based estimation.

dominant when $\partial/\partial t \gg f$). The close agreement between the divergence-based estimate and the simulated upwelling in Case_H indicates that, during the focused period (02:30–08:30 local time), the wind field varied rapidly relative to the inertial period of 18.9 hr.

To identify the timescale range in which the divergence-driven adjustment response is most pronounced and to assess its relative importance against the curl-driven Ekman response, a spectral analysis was conducted over the full simulation period from 23 June to 7 July 2015. The analysis used the time- and spatially varying wind forcing and the corresponding simulated vertical velocity within the boxed region in Case_H. The adjustment and Ekman response terms on the left-hand side of Equation 1 were estimated from the simulated vertical velocity in Case_H (w_H) at 5-min intervals. The velocity was averaged over the upper 10 m, which corresponds to the mean depth of the $\rho = 1{,}025$ kg m^{-3} isopycnal in Case_H, and is expressed as:

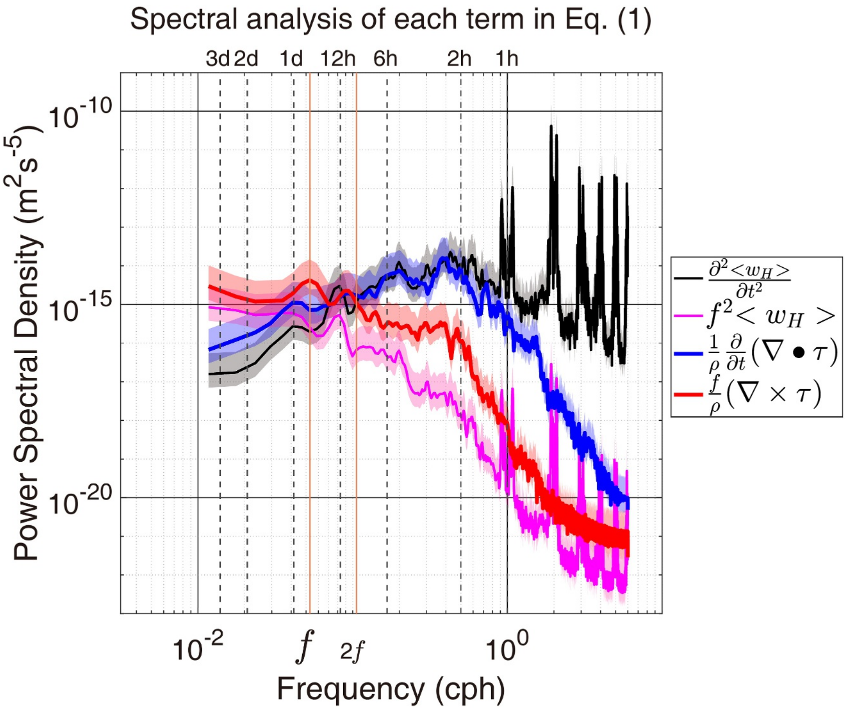

Figure 13. Spectral power of each term in Equation 1 averaged over the boxed region shown in Figure 10. Blue and red lines represent the power spectra of wind forcing terms associated with wind stress divergence and curl, respectively. Black and magenta lines represent the power spectra of the oceanic response terms corresponding to the adjustment process and Ekman dynamics. Shaded areas indicate the 99% confidence intervals.

$$\langle w_H \rangle = \frac{1}{10\ \text{m}} \int_{-10\ \text{m}}^{\text{surface}} w_H\, \text{d}z. \tag{8}$$

Wind forcing terms on the right-hand side were derived from the simulated wind (Section 3.2) interpolated to the same temporal resolution.

Figure 13 shows that the relative importance of divergence and curl changes gradually across timescales relative to the inertial period. The wind stress curl (red) and divergence (blue) forcings intersect near the inertial period. A similar intersection appears in the oceanic responses, where the curl-driven Ekman component (magenta) and the divergence-driven adjustment component (black) also cross near the inertial period. These intersections indicate that, for periods shorter than approximately half the inertial period, divergence-driven adjustment is much stronger and exceeds curl-driven Ekman dynamics by 1–2 orders of magnitude. As the period increases, the relative importance of divergence-driven adjustment decreases. Beyond the inertial period, the divergence-driven oceanic adjustment becomes relatively weaker than the curl-driven Ekman dynamics.

Notably, the maximum spectral power of the divergence forcing (1.6×10^{-14} $\text{m}^2\ \text{s}^{-5}$) is comparable to, or even greater than, that of the curl forcing (4.3×10^{-15} $\text{m}^2\ \text{s}^{-5}$). Together with the improved salinity distribution in Case_H (Figures 4a and 8a), the enhanced SSS associated with divergence-driven upwelling in the bay interior (Figures 10b and 12b), the associated changes in vertical circulation (Figure 11c), and the spectral dominance of divergence-driven adjustment at shorter periods (Figure 13), these results demonstrate that short-timescale wind stress divergence can be a primary driver of bay interior upwelling in small bays and narrow estuaries where local winds vary strongly in space and time.

4. Summary and Discussion

This study investigates wind-driven circulation in a small bay surrounded by complex coastal orography using high-resolution numerical simulations and observations. By accounting for local time-varying winds, spatially varying winds, and Earth's rotation, this study shows that short-timescale wind stress divergence can generate upwelling in the bay interior and modify the SSS distribution in small bays. The key findings are summarized and discussed below.

First, the observed SSS field showed distinct structures, including low-salinity water along the southern coast away from the river mouths and a pronounced north-south salinity gradient. These features were resolved more clearly using the direction-dependent optimal interpolation method than using the direction-independent method, indicating the importance of accounting for direction-dependent spatial correlations in Otsuchi Bay. Repeated observations allowed this directional dependence to be reliably estimated.

Second, time- and spatially varying wind fields generated localized wind stress divergence over the bay interior. These divergence structures varied substantially within the local inertial period of 18.9 hr and were much less evident in the mean D4 wind field. Such structures were also less distinct in the coarser wind fields. These results indicate that the wind stress divergence structures relevant to the bay interior response reflect both short-timescale variability and the small-scale spatial structure of local winds.

Third, time- and spatially varying wind forcing caused upwelling in the interior of the bay. Surface-layer salt budget analysis showed that the improved SSS representation in Case_H compared with Case_U was primarily explained by stronger upwelling in the middle of the bay under spatially varying wind forcing. This upwelling also substantially modified the spatial pattern of estuarine circulation, which is closely linked to vertical transport. While uniform wind forcing confined upwelling and vertical transport to the nearshore region, spatially varying wind forcing enabled substantial vertical transport and modified cross-shore circulation in the interior of the bay, away from the coastline.

Lastly, the bay interior upwelling was driven by wind stress divergence rather than by wind stress curl. Spectral analysis showed that the relative importance of these mechanisms varied continuously across timescales relative to the local inertial period. At timescales shorter than approximately half of the inertial period, vertical motion was primarily induced by divergence-driven oceanic adjustment. As the timescale increased, the contribution from divergence weakened while curl-driven Ekman processes became increasingly important, with the two mechanisms intersecting near the inertial period. At timescales longer than the inertial period, the divergence-driven oceanic adjustment became relatively weaker than the curl-driven Ekman dynamics. Notably, the maximum spectral power of the divergence forcing was comparable to, or even greater than, that of the curl forcing, indicating that short-timescale wind stress divergence can be a primary driver of bay interior upwelling in small bays and narrow estuaries where local winds vary strongly in space and time.

The present results demonstrate that bay interior upwelling in a small bay can be driven by short-timescale wind stress divergence associated with time- and spatially varying wind forcing. This finding indicates that upwelling in small bays is not limited to coastline-confined upwelling or curl-driven Ekman upwelling. Although direct current observations were not available during the simulation period, this conclusion is supported by the comparison between simulated and observed SSS distributions, the surface-layer salt-budget analysis, and the divergence-based vertical-velocity estimate. Further examination of divergence-driven bay interior upwelling based on direct current observations and simulations under a broader range of hydrographic and external forcing conditions, together with further quantification of the relative contributions of wind, tides, and river discharge to the SSS distribution, remains an important topic for future research. As a supplementary check, additional simulations were conducted for two other survey periods representing weaker and stronger stratification conditions. In these additional cases, divergence-driven bay interior upwelling also occurred, and the resulting salinity fields remained broadly consistent with observations, providing additional support for the process examined in the present study (Figure S2 in Supporting Information S1).

Beyond its dynamical importance, divergence-driven bay interior upwelling may also have important implications for material transport in narrow estuaries and small bays. Vertical transport of nutrients and other biogeochemical materials in these systems is often explained by coastline-confined upwelling or curl-driven Ekman upwelling. However, the present results suggest that bay interior vertical transport may also be driven by wind stress divergence, as indicated by the upward transport of high-salinity subsurface water and the resulting surface salinization in Otsuchi Bay. Such processes warrant further investigation, not only from a physical oceanographic perspective but also in the context of biogeochemical dynamics in a broader range of coastal systems surrounded by complex orographic features beyond Otsuchi Bay.

Conflict of Interest

The authors declare no conflicts of interest relevant to this study.

Availability Statement

The processed data and codes used in this study and the numerical model code for KINACO are available in Kim (2026). Weather station data were obtained from the Japan Meteorological Agency database (Japan Meteorological Agency, 2023), and offshore fixed-line oceanographic observation data were obtained from the Iwate Fisheries Technology Center database (Iwate Fisheries Technology Center, 2015). Because the webpages of the original data providers are available only in Japanese, the processed versions of these data sets used in this study are also provided in Kim (2026). ALOS Global Digital Surface Model (AW3D30) data were obtained from the Japan Aerospace Exploration Agency database (Japan Aerospace Exploration Agency, 2021). ERA5 reanalysis data were obtained from the Copernicus Climate Change Service Data Store (Hersbach et al., 2023a, 2023b). The numerical model code for WRF is available from the WRF Model Users' Page (Skamarock et al., 2021). Figures were made with MATLAB (The MathWorks Inc, 2025). Figures 1 and 4 were made together with M_Map: A mapping package for MATLAB, version 1.4 (Pawlowicz, 2020).

Acknowledgments

This work forms a part of the Ph.D. dissertation of Y.J.K. The authors thank T. Adachi at Kagoshima University for providing observational data on river discharges. This work was supported by JSPS KAKENHI Grant JP24H00263, JP22H05204, and JP22H05200. Y.J.K. acknowledges support from the World-leading Innovative Graduate Study Program in Proactive Environmental Studies (WINGS-PES) at The University of Tokyo. Y.M. acknowledges support from the Environment Research and Technology Development Fund of the ERCA (JPMEERF24S12310) by the Ministry of the Environment of Japan. H.S., C.S., and C.R. acknowledge support from NSF (OCE-2148120, OCE-2022846) and NASA (80NSSC21K1524). H.S. thanks support from the Uehiro Center for the Advancement of Oceanography (UC·AO) at the University of Hawai'i at Mānoa.

References

Brasseur, P., Beckers, J. M., Brankart, J. M., & Schoenauen, R. (1996). Seasonal temperature and salinity fields in the Mediterranean Sea: Climatological analyses of a historical data set. *Deep-Sea Research I*, *43*(2), 159–192. https://doi.org/10.1016/0967-0637(96)00012-X

Cáceres, M., Valle-Levinson, A., Sepúlveda, H. H., & Holderied, K. (2002). Transverse variability of flow and density in Chilean fjord. *Continental Shelf Research*, *22*(11–13), 1683–1698. https://doi.org/10.1016/S0278-4343(02)00032-8

Carter, G. S., & Merrifield, M. A. (2007). Open boundary conditions for regional tidal simulations. *Ocean Modelling*, *18*(3–4), 194–209. https://doi.org/10.1016/j.ocemod.2007.04.003

Coogan, J., & Dzwonkowski, B. (2018). Observation of wind forcing effects on estuary length and salinity flux in a river-dominated, microtidal estuary, Mobile Bay, Alabama. *Journal of Physical Oceanography*, *48*(8), 1787–1802. https://doi.org/10.1175/JPO-D-17-0249.1

Egbert, G. D., & Erofeeva, S. Y. (2002). Efficient inverse modeling of barotropic ocean tides. *Journal of Atmospheric and Oceanic Technology*, *19*(2), 183–204. https://doi.org/10.1175/1520-0426(2002)019<0183:EIMOBO>2.0.CO;2

Elliott, A. J. (1978). Observations of the meteorologically induced circulation in the Potomac Estuary. *Estuarine and Coastal Marine Science*, *6*(3), 285–299. https://doi.org/10.1016/0302-3524(78)90017-8

Endoh, M. (1971). Response of a simple two-layer ocean to divergent and rotational wind stress. *Journal of the Oceanographical Society of Japan*, *27*(3), 116–120. https://doi.org/10.1007/BF02109767

Farmer, D. M., & Osborn, T. R. (1976). The influence of wind on the surface layer of a stratified inlet: Part I. Observations. *Journal of Physical Oceanography*, *6*(6), 931–940. https://doi.org/10.1175/1520-0485(1976)006<0931:TIOWOT>2.0.CO;2

Feng, M., Hacker, P., & Lukas, R. (1998). Upper ocean heat and salt balances in response to a westerly wind burst in the western equatorial Pacific during TOGA COARE. *Journal of Geophysical Research*, *103*(C5), 10289–10311. https://doi.org/10.1029/97JC03286

Flather, R. A. (1976). A tidal model of the northwest European continental shelf. *Memories de la Societe Royale des Sciences de Liege*, *6*(10), 141–164.

Geyer, W. R. (1997). Influence of wind on dynamics and flushing of shallow estuaries. *Estuarine, Coastal and Shelf Science*, *44*(6), 713–722. https://doi.org/10.1006/ecss.1996.0140

Gilcoto, M., Largier, J. L., Barton, E. D., Piedracoba, S., Torres, R., Graña, R., et al. (2017). Rapid response to coastal upwelling in a semienclosed bay. *Geophysical Research Letters*, *44*(5), 2388–2397. https://doi.org/10.1002/2016GL072416

Gill, A. E. (1982). *Atmosphere-ocean dynamics*. Academic Press.

Hanawa, K., & Mitsudera, H. (1986). Variation of water system distribution in the Sanriku coastal area. *Journal of Oceanography*, *42*(6), 435–446. https://doi.org/10.1007/BF02110194

Hansen, D. V., & Rattray, M. (1965). Gravitational circulation in straits and estuaries. *Journal of Marine Research*, *23*(2), 104–122. Retrieved from https://elischolar.library.yale.edu/journal_of_marine_research/1048

Hersbach, H., Bell, B., Berrisford, P., Biavati, G., Horányi, A., Muñoz Sabater, J., et al. (2023a). ERA5 hourly data on pressure levels from 1940 to present [Dataset]. *Copernicus Climate Change Service (C3S) Climate Data Store (CDS)*. https://doi.org/10.24381/cds.bd0915c6

Hersbach, H., Bell, B., Berrisford, P., Biavati, G., Horányi, A., Sabater, M., et al. (2023b). ERA5 hourly data on single levels from 1940 to present [Dataset]. *Copernicus Climate Change Service (C3S) Climate Data Store (CDS)*. https://doi.org/10.24381/cds.adbb2d47

Hersbach, H., Bell, B., Berrisford, P., Hirahara, S., Horányi, A., Muñoz-Sabater, J., et al. (2020). The ERA5 global reanalysis. *Quarterly Journal of the Royal Meteorological Society*, *146*(730), 1999–2049. https://doi.org/10.1002/qj.3803

Ishizu, M., Itoh, S., Tanaka, K., & Komatsu, K. (2017). Influence of the Oyashio Current and Tsugaru Warm Current on the circulation and water properties of Otsuchi Bay, Japan. *Journal of Oceanography*, *73*(1), 115–131. https://doi.org/10.1007/s10872-016-0383-z

Iwate Fisheries Technology Center. (2015). Offshore fixed-line oceanographic observation results [Dataset]. (in Japanese) Retrieved from https://www2.suigi.pref.iwate.jp/wp-content/uploads/2017/10/20150716i_research01.pdf

Japan Aerospace Exploration Agency. (2021). ALOS global digital surface model (AW3D30) [Dataset]. *JAXA*. Retrieved from https://www.eorc.jaxa.jp/ALOS/en/dataset/aw3d30/aw3d30_e.htm

Japan Meteorological Agency. (2023). Automated meteorological data acquisition system (AMeDAS) [Dataset]. *JMA*. (in Japanese) Retrieved from https://www.data.jma.go.jp/risk/obsdl/index.php

Johnson, H. K. (1999). Simple expressions for correcting wind speed data for elevation. *Coastal Engineering*, *36*(3), 263–269. https://doi.org/10.1016/S0378-3839(99)00016-2

Kim, Y.-J. (2026). Yoo-Jun/Otsuchi_simulation: v1.2 [Dataset, Software]. *Zenodo*. https://doi.org/10.5281/zenodo.21595772

Kuragano, T., & Kamachi, M. (2000). Global statistical space-time scales of oceanic variability estimated from the TOPEX/POSEIDON altimeter data. *Journal of Geophysical Research*, *105*(C1), 955–974. https://doi.org/10.1029/1999JC900247

Lai, W., & Gan, J. (2023). Variability in coastal downwelling circulation in response to high-resolution regional atmospheric forcing off the Pearl River estuary. *Ocean Science*, *19*(4), 1107–1121. https://doi.org/10.5194/os-19-1107-2023

Largier, J. L. (2020). Upwelling bays: How coastal upwelling controls circulation, habitat, and productivity in bays. *Annual Review of Marine Science*, *12*(1), 415–447. https://doi.org/10.1146/annurev-marine-010419-011020

Li, Y., & Li, M. (2012). Wind-driven lateral circulation in a stratified estuary and its effects on the along-channel flows. *Journal of Geophysical Research*, *117*(C9). https://doi.org/10.1029/2011JC007829

Llebot, C., Rueda, F. J., Solé, J., Artigas, M. L., & Estrada, M. (2014). Hydrodynamic states in a wind-driven microtidal estuary (Alfacs Bay). *Journal of Sea Research*, *85*, 263–276. https://doi.org/10.1016/j.seares.2013.05.010

Matsumura, Y., & Hasumi, H. (2008). A non-hydrostatic ocean model with a scalable multigrid Possion solver. *Ocean Modelling*, *24*(1–2), 15–28. https://doi.org/10.1016/j.ocemod.2008.05.001

Myksvoll, M. S., Sandvik, A. D., Skarðhamar, J., & Sundby, S. (2012). Importance of high resolution wind forcing on eddy activity and particle dispersion in a Norwegian fjord. *Estuarine, Coastal and Shelf Science*, *113*, 293–304. https://doi.org/10.1016/j.ecss.2012.08.019

Nakanishi, M., & Niino, H. (2006). An improved Mellor-Yamada level-3 model: Its numerical stability and application to a regional prediction of advective fog. *Boundary-Layer Meteorology*, *119*(2), 397–407. https://doi.org/10.1007/s10546-005-9030-8

Officer, C. B. (1976). *Physical oceanography of estuaries (and associated coastal waters)*. John Wiley and Sons.

Orlić, M., & Pasarić, Z. (2011). A simple analytical model of periodic coastal upwelling. *Journal of Physical Oceanography*, *41*(6), 1271–1276. https://doi.org/10.1175/JPO-D-10-05000.1

Otobe, H., Onishi, H., Inada, M., Michida, Y., & Terazaki, M. (2009). Estimation of water circulation in Otsuchi Bay, Japan inferred from ADCP observation. *Coastal Marine Science*, *33*(1), 78–86. Retrieved from https://repository.dl.itc.u-tokyo.ac.jp/records/40715

Pawlowicz, R. (2020). M_Map: A mapping package for MATLAB, version 1.4m [Software]. Retrieved from www.eoas.ubc.ca/~rich/map.html

Sakamoto, T. T., Urakawa, L. S., Hasumi, H., Ishizu, M., Itoh, S., Komatsu, T., & Tanaka, K. (2017). Numerical simulation of Pacific water intrusion into Otsuchi Bay, northeast of Japan, with a nested-grid OGCM. *Journal of Oceanography*, *73*, 39–54. https://doi.org/10.1007/s10872-015-0344-y

Scully, M. E., Friedrichs, C., & Brubaker, J. (2005). Control of estuarine stratification and mixing by wind-induced straining of the estuarine density field. *Estuaries*, *28*(3), 321–326. https://doi.org/10.1007/BF02693915

Simpson, J. H., & Sharples, J. (2012). *Introduction to the physical and biological oceanography of shelf seas*. Cambridge University Press.

Skamarock, W. C., Klemp, J. B., Dudhia, J., Gill, D. O., Liu, Z., Berner, J., et al. (2021). A description of the advanced research WRF model version 4.3 (No. NCAR/TN-556+STR). https://doi.org/10.5065/1dfh-6p97

Smagorinsky, J. (1963). General circulation experiments with the primitive equations: I. The basic experiment. *Monthly Weather Review*, *91*(3), 99–164. https://doi.org/10.1175/1520-0493(1963)091<0099:GCEWTP>2.3.CO;2

Soto-Riquelme, C., Pinilla, E., & Ross, L. (2023). Wind influence on residual circulation in Patagonian channels and fjords. *Continental Shelf Research*, *254*, 104905. https://doi.org/10.1016/j.csr.2022.104905

Svendsen, H., & Thompson, R. O. R. Y. (1978). Wind-driven circulation in a fjord. *Journal of Physical Oceanography*, *8*(4), 703–712. https://doi.org/10.1175/1520-0485(1978)008<0703:WDCIAF>2.0.CO;2

Takahashi, D., Miyake, H., Nakayama, T., Kobayashi, N., Kido, K., & Nishida, Y. (2010). Response of a summertime anticyclonic eddy to wind forcing in Funka Bay, Hokkaido, Japan. *Continental Shelf Research*, *30*(13), 1435–1449. https://doi.org/10.1016/j.csr.2010.05.003

Tanaka, K., Komatsu, K., Itoh, S., Yanagimoto, D., Ishizu, M., Hasumi, H., et al. (2017). Baroclinic circulation and its high frequency variability in Otsuchi Bay on the Sanriku ria coast, Japan. *Journal of Oceanography*, *73*(1), 25–38. https://doi.org/10.1007/s10872-015-0338-9

Tanaka, K., Michida, Y., & Komatsu, T. (2008). Numerical experiments on wind-driven circulation and associated transport processes in Suruga Bay. *Journal of Oceanography*, *64*(1), 93–102. https://doi.org/10.1007/s10872-008-0007-3

The MathWorks Inc. (2025). MATLAB R2025a [Software]. *The MathWorks Inc*. Retrieved from https://www.mathworks.com

Umlauf, L., & Burchard, H. (2003). A generic length-scale equation for geophysical turbulence models. *Journal of Marine Research*, *61*(2), 235–265. https://doi.org/10.1357/002224003322005087

Wang, D.-P. (1979). Wind-driven circulation in the Chesapeake Bay, winter 1975. *Journal of Physical Oceanography*, *9*(3), 564–572. https://doi.org/10.1175/1520-0485(1979)009<0564:WDCITC>2.0.CO;2

Xie, X., Li, M., & Boicourt, W. C. (2017). Baroclinic effects on wind-driven lateral circulation in Chesapeake Bay. *Journal of Physical Oceanography*, *47*(2), 433–445. https://doi.org/10.1175/JPO-D-15-0233.1

Zhang, X., Bao, J.-W., Chen, B., & Grell, E. D. (2018). A three-dimensional scale-adaptive turbulent kinetic energy scheme in the WRF-ARW model. *Monthly Weather Review*, *146*(7), 2023–2045. https://doi.org/10.1175/MWR-D-17-0356.1